

Microstructure-Sensitive Fatigue Modeling of AISI 4140 Steel

J. B. Jordon

Department of Mechanical Engineering,
The University of Alabama,
Tuscaloosa, AL 35401

M. F. Horstemeyer

Department of Mechanical Engineering,
Mississippi State University,
Mississippi State, MS 39762;
Center for Advanced Vehicular Systems,
Mississippi State University,
Mississippi State, MS 39762

A microstructure-based fatigue model is employed to predict fatigue damage in 4140 steel. Fully reversed, strain control fatigue tests were conducted at various strain amplitudes and scanning electron microscopy was employed to establish structure-property relations between the microstructure and cyclic damage. Fatigue cracks were found to initiate from particles near the free surface of the specimens. In addition, fatigue striations were found to originate from these particles and grew radially outward. The fatigue model used in this study captured the microstructural effects and mechanics of nucleation and growth observed in this ferrous metal. Good correlation of the number of cycles to failure between the experimental results and the model were achieved. Based on analysis of the mechanical testing, fractography and modeling, the fatigue life of the 4140 steel is estimated to comprise mainly of small crack growth in the low cycle regime and crack incubation in the high cycle fatigue regime. [DOI: 10.1115/1.4025424]

Keywords: fatigue, 4140, modeling, multistage fatigue, microstructure

Introduction

It is well established that the formation of fatigue damage and subsequent evolution can be segmented into four main groups: fatigue crack nucleation; microstructurally small crack (MSC) growth; physically small crack (PSC) growth; and long crack (LC) growth [1]. This formulation and classification of fatigue damage was used as the foundation for the multistage fatigue (MSF) model [2]. The objective of this model was the prediction of fatigue damage arising from various microstructural features. The MSF model showed excellent predictive capabilities in the prediction of fatigue damage in a die-cast A356-T6 aluminum alloy based on microstructural inclusions (casting pores, oxide films, and silicon particles), porosity, dendrite cell size (DCS), and nearest neighbor distance (NND) [2]. Subsequent experiments, micromechanical simulations, and scanning electron microscope (SEM) fractography showed that the main driving force for fatigue damage in this cast aluminum alloy was a combination of several factors, including maximum pore size, DCS, and NND [3]. As such, incubation represented a significant fraction of fatigue life and the scatter in the fatigue experiments was correlated by using the microstructural features directly related to specific test specimens. In an attempt to extend the model to wrought products of other aluminum alloys, the MSF model was adapted to a high strength rolled aluminum alloy [4,5]. Unlike cast alloys, wrought products do not contain pores or significant porosity, and as such, the source of fatigue cracks were found in the 7075-T651 aluminum alloy to be uniformly distributed intermetallics. Micromechanical simulations were also employed to determine the notch root plasticity effects of intermetallic particles versus that of casting pores. Therefore, this microstructure-based fatigue model demonstrated the capability of capturing the fatigue damage, but from a crack growth dominated material. While the scatter in the 7075-T651 aluminum alloy was much less than in the porosity-prevalent cast A356 alloy, the formulation of the model based on segmentation of incubation and crack stages allowed for successful adaptation. Further extension of the MSF model to other alloy systems included correlation to HCP metals, specifically cast and wrought magnesium alloys, with good results [6–9]. In addition, the MSF

model was correlated to Laser Engineered Net Shaping (LENS[®])-processed steel [10]. The experimentally observed fatigue damage in the LENS[®] steel was similar to cast alloys due to the significant/predominant presence of pores and weakly bonded particles.

As the MSF model has evolved to capture fatigue damage evolution arising from various inclusions and microstructurally influenced crack growth regimes for lightweight alloys, the need for a high fidelity fatigue model for traditional metals, like low and medium-carbon steel, still exists. While the current political and environmental atmosphere is pushing research and development of lightweight metals and composites, steel alloys are still widely used due to their high strength, good machinability, and low cost. Steel alloys such as AISI 4140 steel are medium-carbon steels used in a wide range of industrial applications. Specifically, fatigue damage in wrought products like 4140 steel is typically dominated by surface or near-surface initiation sources. As such, surface and heat treatments have a significant impact on fatigue life. Nitriding is a typical surface treatment for 4140 steel that has been shown to improve fatigue performance [11,12]. Thielen et al. studied the strain-controlled, cyclic fatigue behavior of AISI 4140 steel [13,14] and found it to be a function of the tempering temperature: when quenched, the steel showed a hardening effect, while softening occurred when it was tempered at temperatures of 200 °C or higher. The largest softening effect occurred for the material tempered at 400 °C. This hardening was due to dynamic strain aging, while the cyclical softening was due to the rearrangement of dislocation substructures and reduction of dislocation density [14]. Furthermore, heat treatments can also lead to precipitation and clustering of carbon particles that lead to early crack nucleation. Large sources of microstress concentration can lead to more consistent fatigue results.

The purpose of this paper is to extend the MSF model to wrought steel alloys based on the classical incubation and microstructurally small crack growth stages of fatigue damage using an AISI 4140 steel alloy as an example. While research has shown that heat treatments and surface applications can improve the fatigue performance of this particular steel, the true intent of this research is to explore the mechanisms of fatigue for baseline material irrespective of surface treatments. Surface and heat treatments can be naturally incorporated into subsequent model adaptations after the foundation of microstructure-based fatigue modeling is established. As such, structure-property relationships incorporated into the MSF model is presented.

Contributed by the Materials Division of ASME for publication in the JOURNAL OF ENGINEERING MATERIALS AND TECHNOLOGY. Manuscript received May 9, 2013; final manuscript received September 9, 2013; published online February 5, 2014. Assoc. Editor: Irene Beyerlein.

Table 1 Chemical composition of AISI 4140 steel

C	Mn	P	S	Si	Ni	Cr	Mo	Cu	Al	V	Cb	Sn
0.4	0.89	0.01	0.021	0.23	0.05	0.94	0.21	0.12	0.014	0.004	0.002	0.007

Materials and Experiments

AISI 4140 steel is a chromium-molybdenum alloy steel with a 0.4 wt. % C locating this alloy in the medium-carbon steel range. It is commonly used in machinery due to its relatively high hardening sensitivity [15] and corrosion resistance. The chromium content provides good hardenability, and the molybdenum imparts uniformity of hardness and high strength. This grade readily responds to heat treatment and offers good machinability in the heat treated condition. Many different types of this steel are commercially available. However, in this work, a cold drawn and commercially annealed type of 4140 steel was selected. Table 1 lists the chemical composition of the 4140 commercial steel.

The fatigue specimens for this study were machined from bar stock parallel to the extrusion direction. The cylindrical dog-bone-shaped specimens had a gage length of 12 mm and a diameter of 6 mm. In order to reduce machining-surface-influenced fatigue cracks, the shoulder and gage section of each specimen were ground with 320 grit paper in the longitudinal direction until the surface was free of all circumferential machining marks. Fully reversed fatigue tests were conducted under a constant total strain amplitude that ranged from 0.01 to 0.00175 mm/mm. In order to properly control the strain amplitude, an extensometer was employed in the gage region of each specimen for up to 10,000 cycles. If the specimen did not fail by 10,000 cycles, the test was stopped and switched to load-control, and testing was resumed at 30 Hz until failure similar to Ref. [16]. Upon failure, the fracture surfaces were cut from the specimen and mounted for SEM observation. After fatigue crack initiation particles were identified on each fracture surface, energy-dispersive X-ray (EDX) spectroscopy was used to identify the type of the particles.

Multistage Fatigue Model for Ductile Steel

Fundamentals of Multistage Fatigue Modeling. A good summary of the various microstructural features that are the main drivers for fatigue failure associated with a particular materials processing method is summarized in Horstemeyer [17]. The paradigm for the MSF model for fatigue is a microstructurally based approach that comprises three stages of fatigue damage evolution at various scales: incubation, microstructurally small/physically small crack growth, and long crack growth. As such, the total fatigue life can be decomposed as

$$N_{Total} = N_{Inc} + N_{MSC/PSC} + N_{LC} \tag{1}$$

where N_{Total} is the total fatigue life. N_{Inc} is the number of cycles to incubate a crack at an inclusion, which can be a relatively large constituent particle, a large pore, or a cluster of each, or both. The incubated crack extends from the inclusion into the matrix and propagates through a region of the inclusion influence. $N_{MSC/PSC}$ is the number of cycles required for propagation of a microstructurally small/physically small crack. Finally, N_{LC} is number of cycles required for LC propagation to final failure, which depends on the amplitude of loading and the corresponding extent of plasticity ahead of the crack tip. Nucleation is treated in the MSF model as a microscale damage parameter, β , in a modified Coffin–Manson law

$$C_{inc} N_{inc}^z = \beta \tag{2}$$

$$C_{inc} = CNC + z(C_m - CNC) \tag{3}$$

$$CNC = C_n(1 - R) \tag{4}$$

where β is the nonlocal damage parameter around an inclusion, and C_{inc} and α are the linear and exponential coefficients in the modified Coffin–Manson law for incubation. The choice for C_{inc} and α parameters are based on the estimated number of cycles for incubation life, and, R is the load ratio, C_m and C_n are model constants, and z is a localization multiplier [2]. The localization multiplier is nonzero above the microplasticity percolation limit and transitions to unity as the plastic shear strain increases. The localization multiplier is given as

$$z = \frac{l}{D} - \eta_{lim} \tag{5}$$

where D is the size of the critical inclusion that incubates the fatigue crack, l is size of the plastic zone in front of the inclusion, and η_{lim} is the limiting factor. A mean particle diameter of 20 μ m was employed in the MSF model predictions. The limiting factor [2], η_{lim} , defines the transition from constrained plasticity at the micronotch root to unconstrained plasticity at the micronotch root as a function of applied strain amplitude and is governed by the ratio of the plastic zone size to the inclusion size. In cast aluminum alloys, $\eta_{th} = 0.3$ and was also found adequate for LENS[®] processed steel [10].

The physical representation of the damage parameter is related to the nonlocal average maximum plastic shear strain amplitude at an inclusion and is estimated by the following equation:

$$\beta = \frac{\Delta\gamma_{max}^{p*}}{2} = Y[\epsilon_a - \epsilon_{th}]^q, \quad \frac{l}{D} \leq \eta_{lim} \tag{6}$$

$$\beta = \frac{\Delta\gamma_{max}^{p*}}{2} = Y(1 + \xi z)[\epsilon_a - \epsilon_{th}]^q, \quad \frac{l}{D} > \eta_{lim} \tag{7}$$

where ϵ_a is the remotely applied strain amplitude, ϵ_{th} is strain threshold for fatigue incubation [2], q is the exponent in remote strain to local plastic shear strain and ξ is the geometric factor determined in micromechanical simulations [5]. In order to account for mean stress effect, $Y = y_1 + (1 + R)y_2$ is employed, where y_1 and y_2 are model constants. Under fully reversed strain control conditions, $Y = y_1$. The cyclic plastic zone size is calculated using the nonlocal plastic shear strain with respect to the remote loading strain amplitude [5]

$$\frac{l}{D} = \eta_{lim} \frac{\epsilon_a - \epsilon_{th}}{\epsilon_{per} - \epsilon_{th}}, \quad \frac{l}{D} \leq \eta_{lim} \tag{8}$$

$$\frac{l}{D} = 1 - (1 - \eta_{lim}) \left(\frac{\epsilon_{per}}{\epsilon_a} \right)^r, \quad \frac{l}{D} > \eta_{lim} \tag{9}$$

where r is the shape constant for the transition to limited microplasticity [18] and ϵ_{per} is the percolation limit for microplasticity in the vicinity of the inclusion [5]. While the percolation limit can be determined through micromechanical simulations [5], it can also be estimated as $\epsilon_{per} = 0.73\sigma_3^{cyc}/E$, where E is the Young’s modulus [5].

The crack tip displacement range is the driving force for the growth of MSC fatigue cracks, as shown in Eq. (7)

$$\left(\frac{da}{dN}\right)_{\text{MSC}} = \chi(\Delta\text{CTD} - \Delta\text{CTD}_{\text{th}}), \quad a_i = 0.625D \quad (10)$$

where ΔCTD is the crack tip displacement range, $\Delta\text{CTD}_{\text{th}}$ is crack tip displacement range threshold, and χ is a material constant which is typically less than unity and usually taken as 0.32 for aluminum alloys [2]. The threshold crack tip displacement range is on the order of the Burgers' vector of the ferrous matrix which is equal to $2.48 \times 10^{-4} \mu\text{m}$ for pure body-center cubic Fe [19]. The crack tip displacement range is reasonably proportional to applied stress amplitude to a power for high cycle fatigue [2] and to the macroscopic plastic shear strain range in the low cycle fatigue regime, and are a function of the crack tip displacement

$$\Delta\text{CTD} = C_{\text{II}} \left(\frac{\text{GS}}{\text{GS}_0}\right)^{\omega} \left(\frac{\text{GO}}{\text{GO}_0}\right)^{\varpi} \left[\frac{U\Delta\hat{\sigma}}{S_{\text{ut}}}\right]^{\zeta} a + C_{\text{I}} \left(\frac{\text{GS}}{\text{GS}_0}\right)^{\omega} \left(\frac{\text{GO}}{\text{GO}_0}\right)^{\varpi} \left(\frac{\Delta\gamma_{\text{max}}^p}{2}\right)^2 \quad (11)$$

where C_{I} is the low cycle fatigue coefficient, C_{II} and ζ are the high cycle fatigue coefficient and exponent, respectively, and are determined through linear regression, S_{ut} is the ultimate tensile strength, and a is the crack length. While not employed in this work, the model constants GS, GS_0 , GO, and GO_0 and the corresponding exponents (ω and ϖ) are used to capture grain size and crystallographic orientation effects, as illustrated elsewhere [7–9]. The equivalent uniaxial stress amplitude, $\Delta\hat{\sigma} = \bar{\sigma}_a + (1 - \theta)\Delta\sigma_1$, is defined as the linear combination of effective stress amplitude,

$\bar{\sigma}_a = [(3/2)(\Delta\sigma'_{ij}/2)(\Delta\sigma'_{ij}/2)]^{0.5}$, and the maximum principal stress range $\Delta\sigma_1$, where $0 \leq \theta \leq 1$ as the loading parameter introduced by. For mean stress effects on crack growth, the U parameter is employed, where $U = 1/(1 - R)$ is for the case when $R \leq 0$ and $U = 1$ for $R > 0$.

While some previous work employing the MSF model contained long crack growth correlations, in this work and elsewhere [7–9], only incubation and MSC/PSC growth regimes were used due to the relative small size of the specimens used in this study. Also, the long crack growth regime would only constitute a small percentage of the total life in this material, and the long crack growth regime is insensitive to microstructural influences. Finally, the MSC/PSC crack growth laws have been shown to be valid on cracks up to several millimeters in length, which is consistent with the usage of the equations in this study. Table 2 lists the model parameters used to correlate the MSF to fully reversed uniaxial strain-life results for AISI 4140 steel.

Results and Discussion

Microstructure. Optical analyses of the AISI 4140 steel revealed no pre-existing pores within the microstructure of the material. However, some particle inclusions were observed. A representative image of an unetched microstructure is shown in Fig. 1(a), where dark particles are clearly seen. These particles are carbides with an average diameter of $20 \mu\text{m}$. The microstructure of the material (etched condition) consists of a coarse pearlite and pro eutectoid ferrite as shown in Fig. 1(b). These phases observed in this steel are consistent with annealed 4140 steel microstructures.

Table 2 Microstructure-sensitive fatigue modeling parameters for AISI 4140 steel

	Constant	Value	Description
Crack incubation	α	-0.56	Ductility exponent in modified Coffin–Manson law (Eq. (2))
	C_m	0.16	LCF coefficient in modified Coffin–Manson law (Eq. (3))
	C_n	0.1	HCF coefficient in modified Coffin–Manson law (Eq. (4))
	q	2.4	Exponent in remote strain to nonlocal plastic shear strain (Eqs. (6) and (7))
	y_1	140	Constant in remote strain to local plastic shear strain (Eqs. (6) and (7))
	y_2	0	Linear constant in remote strain to local plastic shear strain (Eqs. (6) and (7))
	ξ	2.37	Geometric factor in micromechanics study (Eq. (7))
	r	2	Exponent in micromechanics study (Eq. (9))
Small crack	χ	0.3	Crack growth rate constant (Eq. (10))
	ζ	8	Exponent in small crack growth (Eq. (11))
	C_{I}	60,000	HCF constant in small crack growth (Eq. (11))
	C_{II}	0.02	LCF constant in small crack growth (Eq. (11))
	θ	0	Load path dependent and loading combination parameter (Eq. (11))

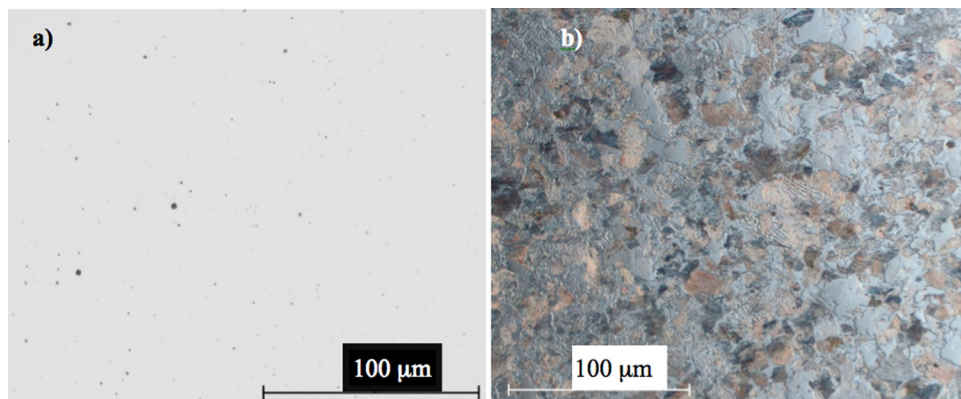


Fig. 1 (a) Unetched micrograph of a representative AISI 4140 showing inclusions, carbides, etc. (b) Typical etched appearance of the AISI 4140 revealing coarse pearlite and proeutectoid phases.

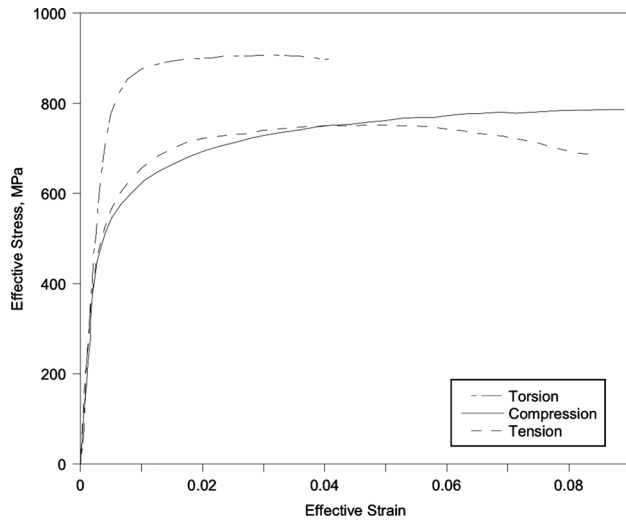


Fig. 2 Effective stress–strain comparison of tension, compression, and torsion of AISI 4140 steel at 300 K and at a strain rate of 0.01/s

Monotonic Stress–Strain Behavior. The effective tensile, compressive, and torsional true stress–strain behavior of AISI 4140 steel is shown in Fig. 2. The AISI 4140 steel exhibited greater yield strength under torsional loading than under tensile or compression loading. However, when comparing tensile with compressive behavior, the tension specimen exhibited nearly symmetric yielding and flow stress up to the point of necking. This reaction is due to the annealing process which relieves the residual stresses that can contribute to the asymmetric behavior observed in other wrought alloys [20].

Strain-Life Behavior. Table 3 lists the results of the fully reversible, constant amplitude, strain-controlled fatigue results of the AISI 4140 steel. Fatigue failure was defined when the maximum cyclic load dropped by 50%, at which point specimens were pulled in tension to provide access to the fatigue crack surface. The strain-life results shown in Fig. 3 display the plateau shape typical of steel alloys. The specimens tested at 0.185% and 0.17% strain amplitude did not fail, indicating that the threshold for microplasticity had been reached [5]. The scatter in the fatigue life was observed to be very low, on the order of 10 in magnitude or less, even for the lowest strain amplitude tested. The following

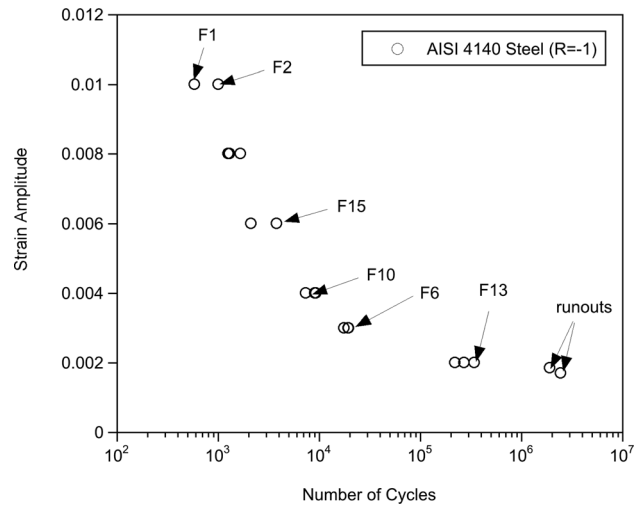


Fig. 3 Strain-life results of AISI 4140 steel tested under fully reversed conditions

specimens were selected for SEM: Specimens #2, #6, #10, and #13.

Cyclic Stress–Strain Behavior. Figure 4 displays the stress amplitude versus the number of cycles for the specimens tested at strain amplitudes ranging from 0.01 to 0.00185. The AISI 4140 steel tested at a 0.01 strain amplitude showed significant cyclic softening, while the 0.00185 strain amplitude showed slight hardening. This transition from cyclic softening is related to the threshold of microplasticity and is a function of the deviation from the proportional limit. Below the proportional limit, the amount of local microplasticity even in the presence of the inclusions is small. At 0.00185 strain amplitude, the threshold for microplasticity was reached, as evident from the sharp knee in the strain-life results shown in Fig. 3. This is further illustrated in Fig. 5, where the amount of plastic strain amplitude increased rapidly above the proportional limit before saturating at a cyclic stress of 500 MPa. An example of the amount cyclic softening from the first cycle to the half-life for a representative 0.004 (specimen F10) strain amplitude is shown in Fig. 6. The hysteresis loops of the strain amplitude of 0.4% exhibited a symmetric decrease in the yield stress from the first to the half-life cycle. As a contrast to the monotonic tension versus compression symmetry

Table 3 Summary of strain-life results of AISI 4140 steel

Specimen ID	Strain amplitude (mm/mm)	Frequency (Hz)	Loading ratio	Failure cycles
F1	0.01	3	-1	588
F2	0.01	3	-1	1008
F3	0.008	3	-1	1266
F14	0.008	3	-1	1303
F16	0.008	3	-1	1665
F4	0.006	3	-1	2127
F15	0.006	3	-1	3762
F11	0.004	3	-1	7390
F10	0.004	3	-1	9075
F5	0.004	3	-1	9310
F8	0.003	3	-1	17,593
F9	0.003	3	-1	19,456
F6	0.003	3	-1	19,683
F12	0.002	3	-1	221,678
F7	0.002	3	-1	271,322
F13	0.002	3	-1	343,075
F17	0.00185	3 (strain control) and 30 (load control)	-1	Did not fail-runout
F16	0.0017	3 (strain control) and 30 (load control)	-1	Did not fail-runout

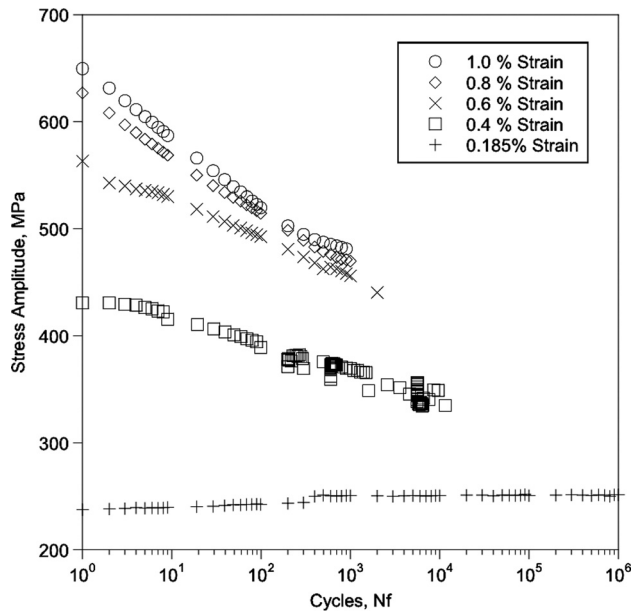


Fig. 4 Stress amplitude versus number of cycles for AISI 4140 steel for the strain amplitude ranging from 1.0% to 0.185%

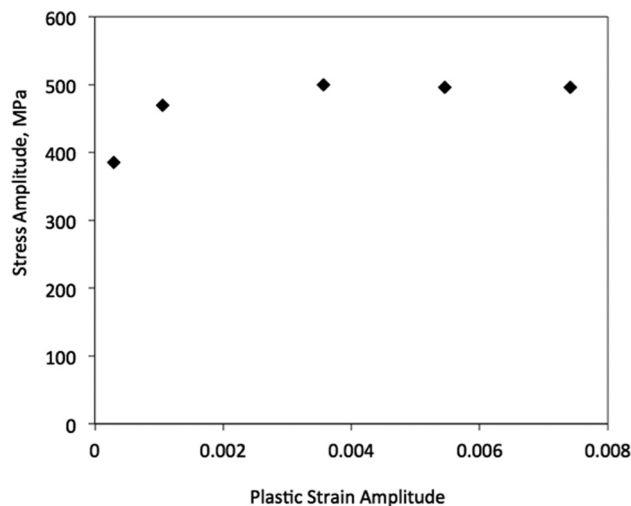


Fig. 5 Cyclic stress amplitude versus plastic strain amplitude for AISI 4140 steel

loading, the cyclic reverse loading showed a significant Bauschinger effect. The pronounced reversed yield asymmetry remained constant from the first cycle to the half-life cycle.

Fatigue Crack Incubation. Fatigue cracks were found to nucleate at the surface of all uniaxial fatigue specimens examined via SEM. The fatigue crack surface was observed to be typically flat and perpendicular to the loading direction. The crack initiation site is indicated at the bottom of Fig. 7(a), where Fig. 7 is an SEM image of specimen F13 tested at a strain amplitude of 0.002. Figure 7(b) shows a higher magnification of the particle that initiated the crack. This particle was approximately $60\ \mu\text{m}$ in diameter. For crack initiation at a high strain amplitude, Fig. 8(a) displays the fatigue crack initiation site for specimen F1, which was tested at an amplitude of 0.01. This particle was nearly $20\ \mu\text{m}$ in diameter, as shown in Fig. 8(b). It is important to note that the specimens subjected to a high strain amplitude, e.g., specimen F1, exhibited multisite crack initiation and growth. In contrast, the specimens tested at low strain amplitudes, e.g., specimen F13,

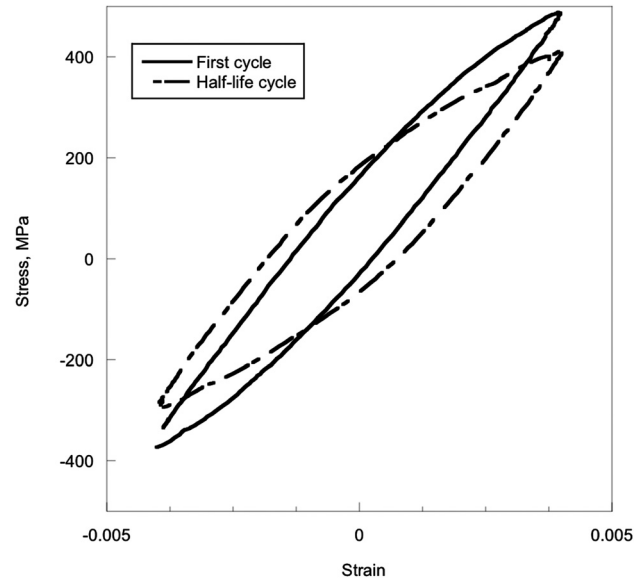


Fig. 6 Representative hysteresis loops of the AISI 4140 steel for first and half-life cycle of the 0.4% strain amplitude. Specimen F10 failed at 9075 cycles.

failed from one dominant crack. Nevertheless, of the six fracture surfaces examined, particles were the source of crack initiation on four of the fatigue specimens examined. On the remaining fatigue fracture surfaces examined, the initiation site contained no particles, thus suggesting that the crack initiation may have occurred due to a persistent slip bands near the specimen surface. Chemical analysis (EDX) aided in indentifying these particles as carbides. Notably, these types of particles are significantly more brittle than the surrounding Pearlite phase and were observed to fracture rather than debond. In fact, no evidence of debonding was observed.

Fatigue Crack Growth. Typical river marks flowing outward from initiation sites at or near the surface were observed on all fatigue specimens examined. The crack grew radially outward from the cracked particle toward the specimen center. Under high magnification of specimen F13, striations were observed on the flat regions near the initiation particle, at a distance of approximately $5\ \mu\text{m}$ from the initiation site (see Fig. 9). As the crack grew away from the initiation site, the striations continued on flat-like regions. Figure 10 shows striations on the flat regions at a distance of approximately $300\ \mu\text{m}$. For the higher strain amplitudes, striations were first observed at a distance much further from the initiation site compared to the lower strain amplitude. The first observed striation for specimen F10 was at approximately $50\ \mu\text{m}$ from the initiation site. In this region, the striations again were found in or on the microcliffs and striations were not found on the flat regions. At a distance of approximately $600\ \mu\text{m}$, the striations became more uniform and were observed on the flat-like regions. Also, the fatigue surface at a distance of $600\ \mu\text{m}$ from the initiation site contained much fewer microcliffs. Figure 11 shows a flat region where striations were observed at a distance of $600\ \mu\text{m}$ from the initiation site.

In order to further characterize the fracture surface, the striation spacing for specimens F6, F10, and F13 versus crack length are shown in Fig. 12. The striation spacing shown in Fig. 12 is the average striation spacing over several striations. The highest striations spacing versus crack length was observed for the 0.004 strain amplitude and the lowest spacing versus crack length was noted for the 0.003 strain amplitude. Also observable from Fig. 12 is the large scatter in the striation spacing, which was observed elsewhere [10]. At approximately $600\text{--}800\ \mu\text{m}$, the striation

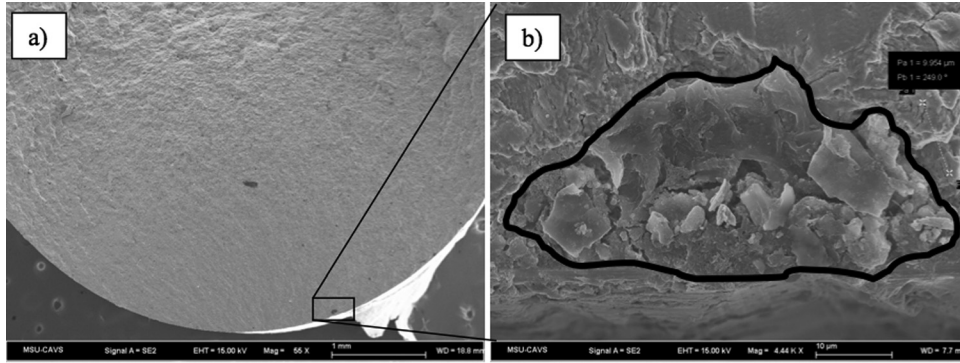


Fig. 7 (a) SEM micrograph of an overview of specimen F13 and (b) a magnified view of the fractured particle that initiated the fatigue crack. Specimen F13 was tested at strain amplitude of 0.002 and failed at 343,075 cycles.

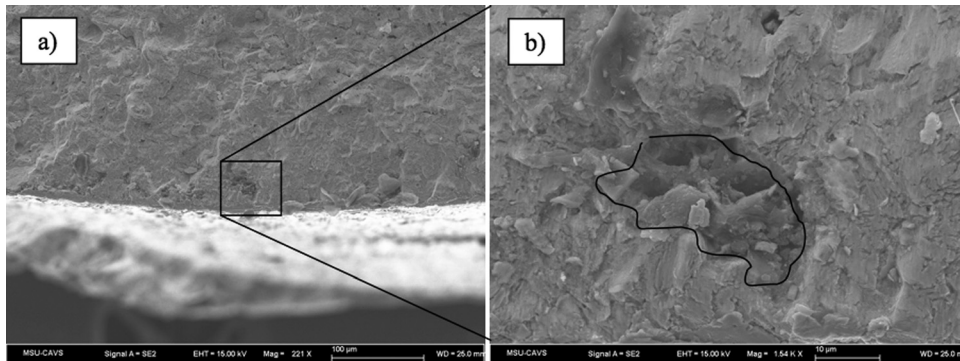


Fig. 8 (a) SEM micrograph of an overview of specimen F1, and a magnified view of the fractured particle (highlighted) that initiated the fatigue crack. (b) Specimen F1 was tested at strain amplitude of 0.01 and failed at 588 cycles.

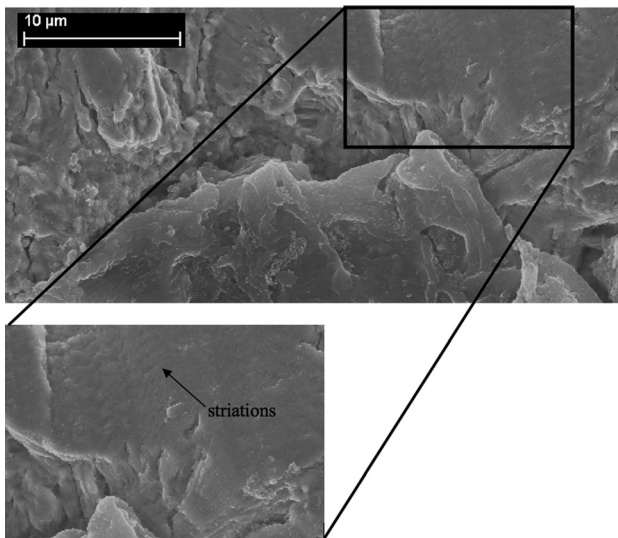


Fig. 9 A magnified view of the particle that initiated the fatigue crack shown in Fig. 7. Striations are clearly seen near the top of the particle as highlighted in this image. Specimen F13 was tested at a strain amplitude of 0.002 and failed at 343,075 cycles.

spacing became nonlinear as the crack size increased. The scatter in the striations is likely due to the microstructural effects of the MSC regime in which the crack growth rate is altered by grain boundaries, crystallographic orientation and carbides. However, striation spacing typically cannot be directly related to the crack

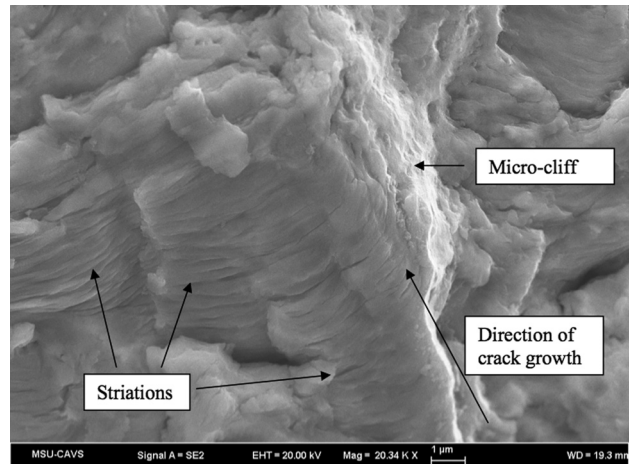


Fig. 10 A magnified view of striations observed on microcliffs of specimen F10 at a distance of 300 μm from the initiation site. Specimen F10 was tested at a strain amplitude of 0.004 and failed at 9075 cycles.

advancement per cycle due to undulations. This is particularly true in the MSC regime where the striation spacing can vary by as much as a factor of 10 due to crack advancement in weaker areas, such as grain boundaries or preferably orientated slip planes. However, it is important to note that the striation spacing for the 0.002 strain amplitude was initially greater than the 0.003 and 0.004 strain amplitudes. This is likely due to the considerable/sizeable particle shown in Fig. 9. This particle was nearly 60 μm in

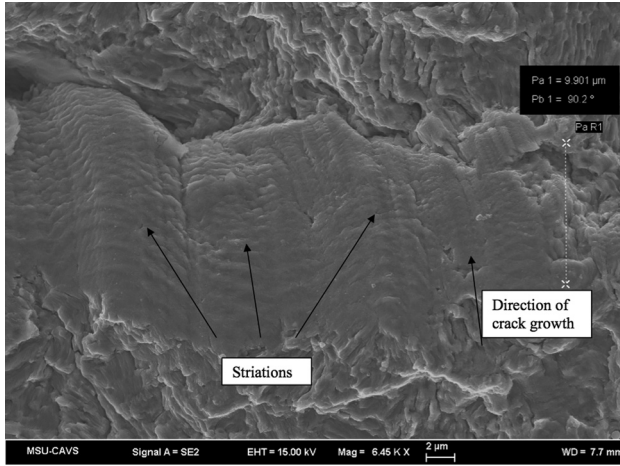


Fig. 11 A magnified view specimen F13 showing a region of striations at 600 μm from the initiation site. Specimen F13 was tested at a strain amplitude of 0.002 and failed at 343,075 cycles.

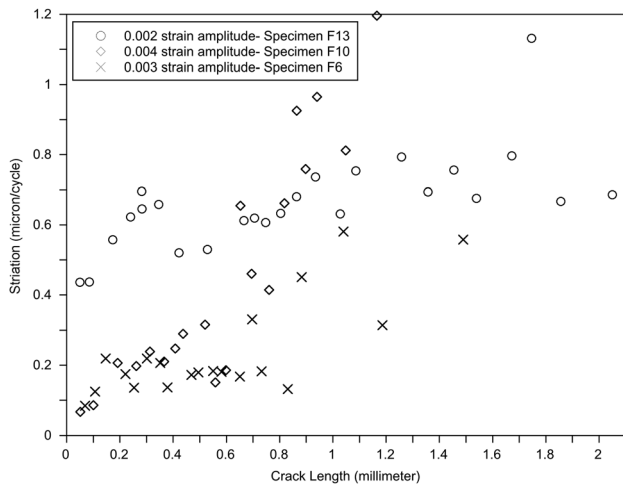


Fig. 12 Striation spacing versus crack length for specimens tested at amplitudes of 0.002, 0.003, and 0.004 strain amplitudes

diameter, which is two to three times greater than the particles that initiated the fatigue cracks on the 0.003 and 0.004 strain amplitude specimens. This large particle for the 0.002 strain amplitude likely caused early crack incubation and a large plastic zone in front of the particle, which led to fast crack propagation. However, as the crack continued to grow, the crack encountered grain boundaries and nonpreferred crystallographic orientations that prevented faster crack growth, even in the presence of an increasing crack driving force. In the other two specimens analyzed for striation spacing, the fatigue cracks initiated from particles that were much smaller than the 0.002 strain amplitude specimen. Thus, the crack growth rate was lower as the crack grew from the particle, but it increased in rate due to the higher applied strain amplitude.

Multistage Fatigue Model Correlations. The MSF model predictions along with the experimental fatigue-life data are shown in Fig. 13. Based on the incubation and MSC/PSC crack regimes, the MSF model showed good correlation to the mean of the fatigue-life results of the AISI 4140 steel. The individual incubation-life and MSC/PSC-life are also shown in Fig. 13. The MSF model supports the conclusion that the fatigue life is

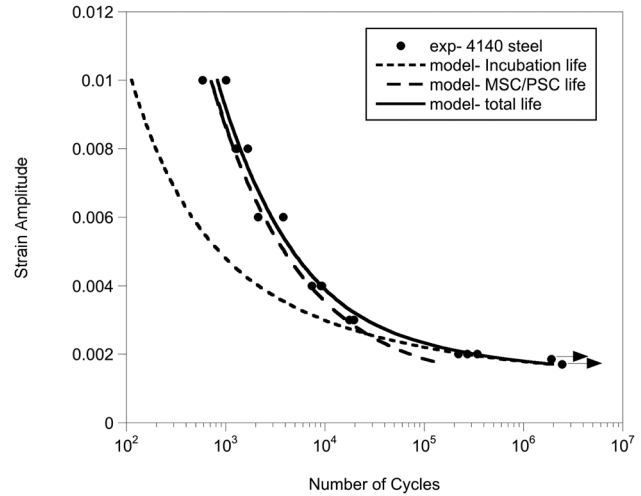


Fig. 13 Experimental AISI 4140 steel strain-life results ($R = -1$) versus the MSF model correlations. Also shown is the incubation and small crack growth predictions of the model.

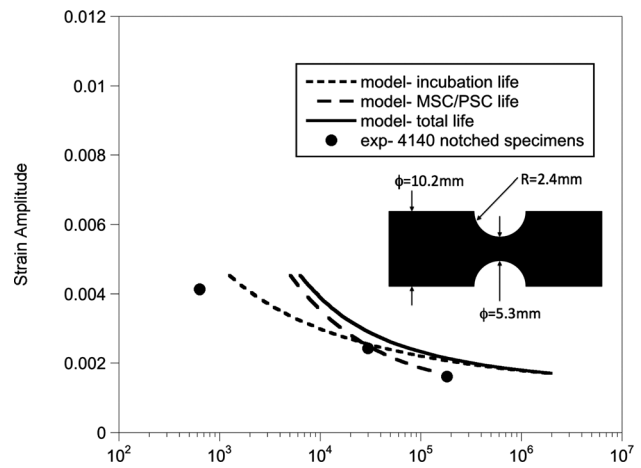


Fig. 14 MSF model comparison to notched fatigue specimens tested under constant displacement. The MSF model predictions were based on finite element internal state variable plasticity results of the notched specimen. An isometric view of the notched cylindrical specimen is shown. Local stress/strain state was used as input for the MSF model.

dominated by the microstructurally small and physically small fatigue crack growth in the low cycle regime (>0.003) and dominated by crack incubation in the high cycle regime (<0.003). Furthermore, experimental results revealed that the fatigue cracks initiated and propagated from fractured carbides, and these fractured particles led to a more consistent fatigue life as exhibited by the strain-life results, as shown in Fig. 13. As such, the crack growth dominated low cycle fatigue and incubation dominated high cycle fatigue modeling approach presented here resulted in predictions that captured the mean fatigue-life of the experimental results.

Multistage Fatigue Model Validation. For validation purposes, several cylindrical notched specimens of the same material as the strain-life specimens were tested under a fully reversed displacement control at 3 Hz. An isometric view of the notched specimen with dimensions is shown in Fig. 14. An extensometer with a 20 mm gage section was employed to provide displacement feedback across the notch region. Three specimens were tested at the following displacement amplitudes: 0.002 mm;

0.0008 mm; 0.00052 mm. The specimens tested at 0.0008 mm and 0.00052 mm displacement amplitudes were switched from a displacement control mode to load-control mode at 10,000 cycles and continued until failure at 30 Hz.

In order to make MSF predictions of the notched specimens, finite element simulations were performed to determine the local stress/strain state due to the presence of the notch. The material model employed in this present study is the internal state variable (ISV) plasticity/damage model introduced by Bammann et al. [21–24] and Horstemeyer and Gokhale [25] and later modified by Horstemeyer and Gokhale [26], and Jordon et al. [27]. The ISV plasticity/damage model constants for AISI 4140 steel were determined from experimental data by using the least-squared best-correlation method. The constants for the kinematic and isotropic hardening equations were selected to produce the best fit of the tensile/compression and torsional data. Three-dimensional finite element simulations were performed with the aforementioned constitutive model and mesh refinement study was employed to determine the appropriate element size. For the boundary conditions, axial displacements identical to the experiments were applied to the finite element simulation for the three tests at the location of 20 mm across the notch. Maximum principle strain theory was employed to account for the multi-axial strain state due to the notch. The maximum principal strain amplitude from the finite element analysis was used as an equivalent uniaxial strain amplitude for the input to the MSF model. Figure 14 shows the comparison of the notched fatigue specimens to the MSF prediction. The MSF showed slightly nonconservative predictions compared to the experimental results. Also shown in the Fig. 14 is the incubation and MSC/PSC crack growth regime. The slightly nonconservative predictions are likely due to the as-machined surface of the notch, which further reduced the number of cycles for incubating a crack. The MSC/PSC life prediction correlated better to all three experimental fatigue-life results compared to the total MSF life or the incubation life. The better fit of the crack growth regime is consistent with a reduced incubation life.

Conclusions

Based on the results of this study of experiments and modeling of fatigue damage in an AISI 4140 steel, the following conclusions are given:

- (1) The strain-life fatigue results of the AISI 4140 steel exhibited relatively low scatter. The scatter observed based on the tests conducted were less than an order of magnitude of scatter.
- (2) Scanning electronic microscopy revealed that the fatigue crack incubation was dominated by the presence of carbon-rich particles located at or near the surface. These particles were found to fracture rather than debond.
- (3) Striations were found within five μm from the incubation site for the specimen tested to failure at the lowest strain amplitude. For the higher strain amplitudes, striations were found within 50 μm of the particle that initiated the fatigue crack. Increasing striation spacing was observed to correlate with increasing applied strain amplitude.
- (4) Good agreement was obtained between the MSF model and experimental strain-life results. The MSF model was found to exhibit nonconservative predictions of the notched specimens based on incubation and small crack life stages. Better correlation was found using solely small crack growth for the notched specimens.

Acknowledgment

The authors would like to thank Andrew Yeldell for conducting the scanning electron microscopy work. This material is based upon work supported by the U.S. Army TACOM Life Cycle

Command under Contract No. W56HZV-08-C-0236 through a subcontract with Mississippi State University, and was performed for the Simulation Based Reliability and Safety (SimBRS) research program. This report was prepared as an account of work sponsored by an agency of the United States Government. Neither the United States Government nor any agency thereof, nor any of their employees, makes any warranty, express or implied, or assumes any legal liability or responsibility for the accuracy, completeness, or usefulness of any information, apparatus, product, or process disclosed, or represents that its use would not infringe privately owned rights. Reference herein to any specific commercial product, process, or service by trade name, trademark, manufacturer, or otherwise does not necessarily constitute or imply its endorsement, recommendation, or favoring by the United States Government or any agency thereof. The views and opinions of authors expressed herein do not necessarily state or reflect those of the United States Government or any agency thereof. Such support does not constitute an endorsement by the Department of Energy of the work or the views expressed herein. UNCLASSIFIED: Dist A. Approved for public release.

References

- [1] Suresh, S., 1998, *Fatigue of Materials*, Cambridge University Press, New York.
- [2] McDowell, D. L., Gall, K., Horstemeyer, M. F., and Fan, J., 2003, "Microstructure-Based Fatigue Modeling of Cast A356-T6 Alloy," *Eng. Fract. Mech.*, **70**, pp. 49–80.
- [3] Jordon, J. B., Horstemeyer, M. F., Yang, N., Major, J. F., Gall, K., Fan, J., and McDowell, D. L., 2010, "Microstructural Inclusion Influence on Fatigue of a Cast A356 Aluminum Alloy," *Metall. Mater. Trans. A*, **41**(2), pp. 356–363.
- [4] Xue, Y., El Kadiri, H., Horstemeyer, M. F., Jordon, J. B., and Weiland, H., 2007, "Micromechanisms of Multistage Crack Growth in a High-Strength Aluminum Alloy," *Acta Mater.*, **55**(6), pp. 1975–1984.
- [5] Xue, Y., McDowell, D. L., Horstemeyer, M. F., Dale, M., and Jordon, J. B., 2007, "Microstructure-Based Multistage Fatigue Modeling of Aluminum Alloy 7075-T651," *Eng. Fract. Mech.*, **74**, pp. 2810–2823.
- [6] Xue, Y., Horstemeyer, M. F., McDowell, D., El Kadiri, H., and Fan, J., 2007, "Microstructure-Based Multistage Fatigue Modeling of a Cast AE44 Magnesium Alloy," *Int. J. Fatigue*, **29**, pp. 666–676.
- [7] Jordon, J. B., Gibson, J. B., Horstemeyer, M. F., Kadiri, H. E., Baird, J. C., and Luo, A. A., 2011, "Effect of Twinning, Slip, and Inclusions on the Fatigue Anisotropy of Extrusion-Textured AZ61 Magnesium Alloy," *Mater. Sci. Eng. A*, **528**(22), pp. 6860–6871.
- [8] Rettberg, L. H., Jordon, J. B., Horstemeyer, M. F., and Jones, J. W., 2012, "Low-Cycle Fatigue Behavior of Die-Cast Mg Alloys AZ91 and AM60," *Metall. Mater. Trans. A*, **43**(7), pp. 2260–2274.
- [9] Lugo, M., Jordon, J. B., Solanki, K. N., Hector, L. G., Jr., Bernard, J. D., Luo, A. A., and Horstemeyer, M. F., 2013, "Role of Different Material Processing Methods on the Fatigue Behavior of AZ31 Magnesium Alloy," *Int. J. Fatigue*, **52**, pp. 131–143.
- [10] Xue, Y., Pascu, A., Horstemeyer, M. F., Wang, L., and Wang, P. T., 2010, "Microstructural Effects on Cyclic Plasticity and Fatigue of LENSTM-Processed Steel," *Acta Mater.*, **58**(11), pp. 4029–4038.
- [11] Celik, A., and Karadeniz, S., 1995, "Improvement of the Fatigue Strength of AISI 4140 Steel by an Ion Nitriding Process," *Surf. Coat. Technol.*, **72**(3), pp. 169–173.
- [12] Limodin, N., and Verreman, Y., 2006, "Fatigue Strength Improvement of a 4140 Steel by Gas Nitriding: Influence of Notch Severity," *Mater. Sci. Eng. A*, **435–436**, pp. 460–467.
- [13] Thielen, P. N., and Fine, M. E., 1975, "Fatigue Crack Propagation in 4140 Steel," *Metall. Trans. A*, **6**, pp. 2133–2140.
- [14] Thielen, P. N., Fine, M. E., and Fournelle, R. A., 1976, "Cyclic Stress Strain Relations and Strain-Controlled Fatigue of 4140 Steel," *Acta Metall.*, **24**(1), pp. 1–10.
- [15] Steiner, R., 1990, *ASM Handbook*, Vol. 1: Properties and Selection; Irons, Steels, and High Performance Alloys, ASM International, Materials Park, OH, p. 140.
- [16] Begum, S., Chen, D. L., Xu, S., and Luo Alan A., 2008, "Strain-Controlled Low-Cycle Fatigue Properties of a Newly Developed Extruded Magnesium Alloy," *Metall. Mater. Trans. A*, **39**, pp. 3014–3026.
- [17] Horstemeyer, M. F., 2012, *Integrated Computational Materials Engineering (ICME) for Metals: Reinvigorating Engineering Design With Science*, Wiley Press, Hoboken, NJ.
- [18] Hayhurst, D. R., Leckie F. A., and McDowell, D. L., 1985, "Damage Growth Under Nonproportional Loading," ASTM, Philadelphia, Paper No. ASTM STP 853, pp. 688–699.
- [19] Jordon, J. B., Horstemeyer, M. F., Solanki, K., and Xue, Y., 2007, "Damage and Stress State Influence on the Bauschinger Effect in Aluminum Alloys," *Mech. Mater.*, **39**(10), pp. 920–931.

- [20] Peeters, B., Seefeldt, M., Teodosiu, C., Kalidindi, S. R., Van Houtte, P., and Aernoudt, E., 2001, "Work-Hardening/Softening Behaviour of BCC Polycrystals During Changing Strain Paths: I. An Integrated Model Based on Substructure and Texture Evolution, and Its Prediction of the Stress-Strain Behaviour of an IF Steel During Two-Stage Strain Paths," *Acta Mater.*, **49**(9), pp. 1607–1619.
- [21] Bammann, D. J., and Aifantis, E. C., 1987, "A Model for Finite-Deformation Plasticity," *Acta Mech.*, **69**, pp. 97–117.
- [22] Bammann, D. J., and Aifantis, E. C., 1989, "A Damage Model for Ductile Metals," *Nucl. Eng. Des.*, **116**, pp. 355–362.
- [23] Bammann, D. J., Chiesa, M. L., Horstemeyer, M. F., and Weingarten, L. I., 1993, "Failure in Ductile Materials Using Finite Element Methods," *Structural Crashworthiness and Failure*, Elsevier Applied Science, London, Chap. 1.
- [24] Bammann, D. J., Chiesa, M. L., and Johnson, G. C., 1996, "Modeling Large Deformation and Failure in Manufacturing Processes," *Theoretical and Applied Mechanics*, Tatsumi, Wannabe, and Kambe, eds., Elsevier Science, London, pp. 359–376.
- [25] Horstemeyer, M. F., and Gokhale, A. M., 1999, "A Void-Crack Nucleation Model for Ductile Metals," *Int. J. Solids Struct.*, **36**, pp. 5029–5055.
- [26] Horstemeyer, M. F., Lathrop, J., Gokhale, A. M., and Dighe, M., 2000, "Modeling Stress State Dependent Damage Evolution in a Cast Al-Si-Mg Aluminum Alloy," *Theor. Appl. Fract. Mech.*, **33**, pp. 31–47.
- [27] Jordon, J. B., Horstemeyer, M. F., Bernard, J. D., Solanki, K., and Berry, J. T., 2009, "Damage Characterization and Modeling of a 7075-T651 Aluminum Plate," *Mater. Sci. Eng. A*, **527**(1–2), pp. 169–178.